

CrossMark  
click for updatesCite this: *Chem. Sci.*, 2015, 6, 894

# Durable hydrogen evolution from water driven by sunlight using (Ag,Cu)GaSe<sub>2</sub> photocathodes modified with CdS and CuGa<sub>3</sub>Se<sub>5</sub><sup>†</sup>

Li Zhang,<sup>a</sup> Tsutomu Minegishi,<sup>a</sup> Mamiko Nakabayashi,<sup>b</sup> Yohichi Suzuki,<sup>c</sup> Kazuhiko Seki,<sup>c</sup> Naoya Shibata,<sup>b</sup> Jun Kubota<sup>a</sup> and Kazunari Domen<sup>\*a</sup>

The photoelectrochemical properties of (Ag,Cu)GaSe<sub>2</sub> (ACGSe) modified by deposition of CdS and CuGa<sub>3</sub>Se<sub>5</sub> layers were investigated. The CdS and CuGa<sub>3</sub>Se<sub>5</sub> layers formed p–n junctions with an appropriate band diagram on the surface of the electrode and they clearly increased the cathodic photocurrent and onset potential. The Pt, CdS, and CuGa<sub>3</sub>Se<sub>5</sub> modified ACGSe (Pt/CdS/CuGa<sub>3</sub>Se<sub>5</sub>/ACGSe) with an appropriate thickness of CuGa<sub>3</sub>Se<sub>5</sub> layers (ca. 100 nm) showed a cathodic photocurrent of 8.79 mA cm<sup>-2</sup> at 0 V<sub>RHE</sub> and an onset potential of 0.62 V<sub>RHE</sub> (defined as cathodic photocurrent of 1.0 mA cm<sup>-2</sup>) under simulated sunlight irradiation in 0.1 M Na<sub>2</sub>HPO<sub>4</sub> (pH 10). Pt/CdS/CuGa<sub>3</sub>Se<sub>5</sub>/ACGSe showed durable cathodic current under the observed reaction conditions and hydrogen was evolved for about 20 days.

Received 4th August 2014  
Accepted 3rd September 2014

DOI: 10.1039/c4sc02346c

www.rsc.org/chemicalscience

## Introduction

Sustainable energy supply is one of the greatest challenges facing human society today.<sup>1,2</sup> Global energy consumption was equivalent to ca. 1.5 × 10<sup>11</sup> TW in 2008, and is predicted to double by 2050 and triple by 2100.<sup>3</sup> Utilization of solar energy appears to be our best option for addressing the decreased availability of finite fossil fuels and the increase of anthropogenic carbon dioxide emissions, because the solar energy reaching the Earth (1.3 × 10<sup>17</sup> TW) is roughly four orders of magnitude greater than the global energy consumption.<sup>4</sup>

Solar energy generation through solar cells is one fascinating way to harvest energy from the sun. However, solar cells can generate electricity only during daytime and only on sunny days, and they should be coupled with efficient energy storage technology to overcome the diurnal intermittency of sunlight.<sup>5</sup> Solar-driven water splitting for hydrogen production is potentially one of the most sustainable and efficient energy storage technologies.<sup>4,6</sup> Storable and renewable hydrogen produced by solar-driven water splitting can be used directly to obtain mechanical energy using a combustion engine or be converted

into electricity using a fuel cell as a clean fuel, whenever and wherever necessary.

Photoelectrochemical (PEC) water splitting, which integrates sunlight absorption and water electrolysis into a single semiconductor electrode, presents an attractive and efficient solution for solar-driven hydrogen production.<sup>7–9</sup> The search for a single-photoelectrode PEC cell capable of bias-free overall water splitting with sufficient efficiency and adequate stability has proven to be quite difficult.<sup>10</sup> A dual-photoelectrode PEC cell that consists of a photoanode and a photocathode with overlapped band gaps covering the oxygen evolution and hydrogen evolution potentials in side-by-side or top-to-bottom configurations, has been proposed as one of the most effective solutions with the potential to achieve solar-to-hydrogen (STH) conversion efficiencies of larger than 10% for large-scale applications.<sup>10–12</sup>

To drive efficient overall water splitting on a dual-photoelectrode PEC cell, a sufficiently large photocurrent at the intersection of the photocurrent–potential curves of the respective electrodes is necessary. Lower and higher onset potentials of the photocurrents from the photoanode and photocathode, respectively, are required in order to achieve efficient water splitting. Extensive research efforts have been devoted to photoanodes based on metal oxides (TiO<sub>2</sub>,<sup>13</sup> α-Fe<sub>2</sub>O<sub>3</sub>,<sup>14,15</sup> BiVO<sub>4</sub>,<sup>16,17</sup> WO<sub>3</sub>,<sup>18,19</sup> and ZnO<sup>20</sup>), metal (oxy)nitrides (TaON,<sup>21</sup> Ta<sub>3</sub>N<sub>5</sub>,<sup>22,23</sup> BaTiO<sub>2</sub>N,<sup>24</sup> and LaTiO<sub>2</sub>N<sup>25</sup>), and n-type Si.<sup>26,27</sup> Relatively fewer studies have focused on photocathodes.<sup>28–33</sup> Single-crystalline p-type phosphides (InP<sup>28</sup> and GaInP<sub>2</sub> (ref. 29)) have been reported to be highly efficient photocathodes for hydrogen evolution. As Earth-abundant and inexpensive semiconductor materials, p-type Cu<sub>2</sub>O<sup>30,31</sup> and p-type Si<sup>32,33</sup>

<sup>a</sup>Department of Chemical System Engineering, The University of Tokyo, 7-3-1 Hongo, Bunkyo-ku, Tokyo, 113-8656, Japan. E-mail: domen@chemsys.t.u-tokyo.ac.jp; Fax: +81-3-5841-8838; Tel: +81-3-5841-1652

<sup>b</sup>Institute of Engineering Innovation, The University of Tokyo, 2-11-16 Yayoi, Bunkyo-ku, Tokyo 113-8656, Japan

<sup>c</sup>NRI, National Institute of Advanced Industrial Science and Technology (AIST), AIST Tsukuba Central 5, Higashi 1-1-1, Tsukuba, Ibaraki 305-8565, Japan

<sup>†</sup> Electronic supplementary information (ESI) available. See DOI: 10.1039/c4sc02346c



have been investigated as photocathodes for hydrogen evolution.

As one category of efficient sunlight-absorbing materials, I-III-VI<sub>2</sub> chalcogenides (I = Cu; III = In, Ga; VI = S, Se) have emerged as a leading class of thin film solar cell materials, due to their tunable band gap (*ca.* 1.0–2.4 eV), high photo-absorption coefficients (*ca.* 10<sup>5</sup> cm<sup>-1</sup>) and usability in the polycrystalline state.<sup>34–37</sup> All of these beneficial properties have encouraged researchers to study the application of I-III-VI<sub>2</sub> chalcogenides as photoelectrodes for PEC water splitting. Among the materials tested, CuGaSe<sub>2</sub> (CGSe), with a direct band gap of 1.65 eV, is one of the more promising candidates as a photocathode for hydrogen evolution,<sup>38–40</sup> because it can efficiently utilize a large portion of visible sunlight (absorption edge *ca.* 750 nm). Assuming an incident-photon-to-current-conversion efficiency (IPCE) of 100%, a CGSe photocathode can generate a photocurrent of 24 mA cm<sup>-2</sup> above the absorption edge against AM 1.5G light (ASTM G173-03).<sup>41</sup>

Marsen *et al.* reported that a CGSe photocathode worked stably for hydrogen evolution in a strongly acidic electrolyte (0.5 M H<sub>2</sub>SO<sub>4</sub>), and they obtained a saturated photocurrent of 10.6 mA cm<sup>-2</sup> at -0.9 V<sub>SCE</sub> (*i.e.*, -0.66 V<sub>RHE</sub>) under simulated sunlight, although the onset potential was relatively low (*ca.* 0.136 V<sub>RHE</sub>).<sup>38</sup> The low onset potential of CGSe photocathodes is due to its valence-band maximum (VBM) position, which is too shallow compared to the oxygen evolution potential in PEC water splitting. For Cu-based chalcogenide photocathodes, surface modification using a thin layer of n-type CdS to form a p-n heterojunction is an effective way to obtain higher onset potentials and cathodic photocurrents.<sup>39,40,42–45</sup> Yokoyama *et al.* reported that CdS modification of Cu(In,Ga)Se<sub>2</sub> and Cu<sub>2</sub>ZnSnS<sub>4</sub> photocathodes clearly increased the photocurrents and onset potentials for hydrogen evolution.<sup>42,43</sup> Ikeda *et al.* demonstrated an appreciable enhancement of the PEC response on a CuInS<sub>2</sub> photocathode by the introduction of a thin CdS layer.<sup>44,45</sup> Moriya *et al.* recently reported that a CGSe photocathode modified with CdS and Pt showed a marked increase in photocurrent and onset potential, owing to the enhanced charge separation by the formation of a p-n heterojunction, where Pt/CdS/CGSe reached a hypothetical half-cell solar-to-hydrogen efficiency (HC-STH) of 0.83% at 0.2 V<sub>RHE</sub>.<sup>39</sup> More recently, the authors have reported an improvement of the CGSe electrodes by the partial substitution of Cu for Ag.<sup>46</sup> The resulting (Ag,Cu)GaSe<sub>2</sub> (ACGSe) electrodes modified with CdS and Pt showed an enhanced HC-STH (1.22% at 0.3 V<sub>RHE</sub>), since ACGSe has a larger grain size and a more positive VBM potential than CGSe. However, the measured efficiency of the Pt/CdS/ACGSe photocathode was still lower than that expected on the basis of the band gap of ACGSe (*ca.* 1.65 eV) and its flat-band potential. One possible reason for this might be a large amount of carrier recombination at the CdS/ACGSe interface due to the high defect density resulting from the large lattice mismatch, in addition to the unfavorably large band offset, as is commonly encountered in the case of CdS/CGSe interfaces in solar cells.<sup>47,48</sup>

Introducing a surface modification layer to form more desirable band alignments for the CdS/ACGSe heterojunction might help to reduce interfacial recombination, and thus

enhance hydrogen evolution on the Pt/CdS/ACGSe photocathode. The ordered defect compound (ODC) of CGSe, CuGa<sub>3</sub>Se<sub>5</sub>, has emerged as a potential candidate for this purpose, owing to the fact that its band gap (*ca.* 1.85 eV) is larger than that of CGSe (or ACGSe) due to deepening of the VBM potential,<sup>49,50</sup> and it is structurally similar to CGSe (or ACGSe) except for the periodic presence of (2V<sub>Cu</sub><sup>-</sup> + Ga<sub>Cu</sub><sup>2+</sup>) defect pairs (*i.e.*, a single defect pair for each 5 units of CGSe).<sup>51</sup> Rusu *et al.* studied the electronic properties of ODCs of CGSe, namely CuGa<sub>3</sub>Se<sub>5</sub> and CuGa<sub>5</sub>Se<sub>8</sub>, and showed that they had deeper VBM positions than CGSe.<sup>49</sup> Kim *et al.* investigated the structural and PEC properties of CuGa<sub>3</sub>Se<sub>5</sub> (ref. 50 and 52) and found that CuGa<sub>3</sub>Se<sub>5</sub> had p-type conductivity and a deeper VBM position than CGSe. After Pt modification, they observed a high onset potential (*ca.* 1.1 V<sub>RHE</sub>) on the CuGa<sub>3</sub>Se<sub>5</sub> photocathode under simulated sunlight. However, the HC-STH for both Pt/CuGa<sub>3</sub>Se<sub>5</sub> and Pt/ZnS/H<sub>2</sub>:CuGa<sub>3</sub>Se<sub>5</sub> was less than 0.4%, presumably owing to the very small grain size in CuGa<sub>3</sub>Se<sub>5</sub>, which made it difficult to form a p-n junction because of strong Zn diffusion across the grain boundaries.

In the present study, the PEC and structural properties of CuGa<sub>3</sub>Se<sub>5</sub>-modified ACGSe (CuGa<sub>3</sub>Se<sub>5</sub>/ACGSe) thin film photocathodes decorated with CdS and Pt were investigated. It was found that Pt- and CdS-modified CuGa<sub>3</sub>Se<sub>5</sub>/ACGSe (Pt/CdS/CuGa<sub>3</sub>Se<sub>5</sub>/ACGSe) photocathodes showed a significantly higher photocurrent and onset potential than Pt/CdS/ACGSe photocathodes.

## Experimental

### Preparation of the CuGa<sub>3</sub>Se<sub>5</sub>/ACGSe thin films

CuGa<sub>3</sub>Se<sub>5</sub>/ACGSe thin films were prepared on Mo/Ti/SLG (SLG: soda lime glass) substrates by vacuum co-evaporation using a molecular beam epitaxy (MBE) system. The Mo/Ti/SLG substrates were prepared by radio frequency (RF) magnetron sputtering (see ESI†). Knudsen cells loaded with high-purity elemental sources of Ag (6 N), Cu (5 N), Ga (6 N) and Se (6 N) were placed in the vacuum chamber of the MBE system having a base pressure of *ca.* 1 × 10<sup>-6</sup> Pa. Each of these cells consisted of a crucible, heating filaments, thermocouple, shutter and cooling line. The deposition rates for Ag, Cu, Ga and Se were monitored by an *in situ* quartz crystal microbalance (QCM) system and controlled by adjusting the source temperature. ACGSe films with a Ag/(Cu + Ag) ratio of *ca.* 5% were prepared by a two-step deposition method,<sup>39,46</sup> in which the ACGSe thin films were first deposited at a relatively low substrate temperature of 450 °C for 10 min, followed by deposition at 550 °C for 90 min. The deposition rates for Ag, Cu and Ga were 0.03, 0.28 and 0.06 Å s<sup>-1</sup> with a fluctuation of ±0.01 Å s<sup>-1</sup> for each, resulting in ACGSe films with a Ag/(Cu + Ag) ratio of *ca.* 5% and a slight group I deficiency (Cu + Ag)/Ga of *ca.* 0.85. The deposition rate for Se was fixed at 8.00 ± 1.00 Å s<sup>-1</sup> to ensure Se-rich conditions. For the CuGa<sub>3</sub>Se<sub>5</sub> modified samples, CuGa<sub>3</sub>Se<sub>5</sub> was deposited onto the grown ACGSe at 550 °C for 10 to 20 min under H<sub>2</sub>-mediated conditions.<sup>52</sup> Pure H<sub>2</sub> gas (5 N) was continuously introduced into the vacuum chamber and maintained at a constant pressure of *ca.* 5.0 × 10<sup>-3</sup> Pa by adjusting



the needle valve. The deposition rates for Cu and Ga were 0.12 and 0.06 Å s<sup>-1</sup> with a fluctuation of ±0.01 Å s<sup>-1</sup> for both elements. The deposition rate for Se was 4.00 ± 1.00 Å s<sup>-1</sup>, with a Se/metal flux ratio of *ca.* 4. Before the fabrication of the electrodes, CdS layers were formed on the surface of prepared CuGa<sub>3</sub>Se<sub>5</sub>/ACGSe films by the chemical bath deposition (CBD) method (see ESI†).

### Photoelectrochemical measurements

The prepared CdS/CuGa<sub>3</sub>Se<sub>5</sub>/ACGSe thin film samples were fabricated into electrodes and then surface-modified with Pt as a hydrogen evolution catalyst by PEC deposition (see ESI†). PEC measurements were performed using a typical 3-electrode setup consisting of a specimen, a coiled Pt wire, and an Ag/AgCl electrode in a saturated aqueous KCl solution as the working, counter, and reference electrodes, respectively. The potential of the working electrode was controlled by a potentiostat (Hokuto Denko, HSV-100). An aqueous solution of 0.1 M Na<sub>2</sub>HPO<sub>4</sub> (99%, Wako) with the pH adjusted to 10 by NaOH addition was employed as the electrolyte. All PEC measurements were conducted under an Ar-purged atmosphere.

Photocurrent densities were measured under simulated sunlight illumination using an AM 1.5G solar simulator (XES-40S2-CE, San-ei Electric), as shown in Fig. S1 in ESI†. The wavelength dependence of the IPCE was measured under monochromatic light from a Xe lamp (Max-301, Asahi Spectra) equipped with band-pass filters (full width at half maximum (FWHM) ≈ 10 nm) and an optical fiber. Monochromatic light intensities were measured using a calibrated Si photodiode (S2281-01, Hamamatsu).

## Results and discussion

### PEC properties of the Pt/CdS/CuGa<sub>3</sub>Se<sub>5</sub>/ACGSe photocathodes

Current–potential (*I*–*E*) curves for the Pt/CdS/CuGa<sub>3</sub>Se<sub>5</sub>/ACGSe electrodes with various deposition times for the CuGa<sub>3</sub>Se<sub>5</sub> layer are shown in Fig. 1a, and the photocurrents at 0 V<sub>RHE</sub> and onset potentials are plotted against the CuGa<sub>3</sub>Se<sub>5</sub> deposition time in Fig. 1b. All of the Pt/CdS/CuGa<sub>3</sub>Se<sub>5</sub>/ACGSe samples showed an enhanced cathodic photocurrent compared to Pt/CdS/ACGSe, with a small photocurrent being observed for an applied potential of >0.6 V<sub>RHE</sub>. The Pt/CdS/CuGa<sub>3</sub>Se<sub>5</sub>/ACGSe electrode with CuGa<sub>3</sub>Se<sub>5</sub> deposited for 15 min showed the highest cathodic photocurrent (8.79 mA cm<sup>-2</sup> at 0 V<sub>RHE</sub>), and an onset potential of *ca.* 0.62 V<sub>RHE</sub> (defined as a cathodic photocurrent of 1.0 mA cm<sup>-2</sup>) based on the averaged values from three samples (see Fig. S2 in ESI†). Compared with Pt/CdS/ACGSe, which showed a cathodic photocurrent of 7.26 mA cm<sup>-2</sup> at 0 V<sub>RHE</sub> and an onset potential of 0.48 V<sub>RHE</sub>, this Pt/CdS/CuGa<sub>3</sub>Se<sub>5</sub>/ACGSe sample showed a clear increase in photocurrent density over the entire potential range below the onset potential (see Fig. 1c), and, more importantly, a positive shift in the onset potential (*ca.* 140 mV). For Pt/CdS/CuGa<sub>3</sub>Se<sub>5</sub>/ACGSe, the maximum HC-STH was 1.81% at 0.36 V<sub>RHE</sub> (see Fig. S3 in ESI†), while for Pt/CdS/ACGSe, it was 1.02% at 0.32 V<sub>RHE</sub>. It should be noted that the HC-STH for Pt/CdS/ACGSe is almost in agreement with the

reported value.<sup>46</sup> The observed small photocurrent for all of the Pt/CdS/CuGa<sub>3</sub>Se<sub>5</sub>/ACGSe samples at applied potential of >0.6 V<sub>RHE</sub> was probably due to the photoexcited electrons generated in the CuGa<sub>3</sub>Se<sub>5</sub> layer.<sup>50</sup> The clear increase in onset potential on Pt/CdS/CuGa<sub>3</sub>Se<sub>5</sub>/ACGSe photocathodes can be ascribed to the contribution of the CuGa<sub>3</sub>Se<sub>5</sub> layers. Possible mechanisms for the enhancement of the photocurrent and onset potential will be discussed below.

The measured IPCE spectra of Pt/CdS/CuGa<sub>3</sub>Se<sub>5</sub>/ACGSe and Pt/CdS/ACGSe are shown in Fig. 2. Pt/CdS/CuGa<sub>3</sub>Se<sub>5</sub>/ACGSe showed a higher efficiency than Pt/CdS/ACGSe at all measured wavelengths. The IPCE for Pt/CdS/CuGa<sub>3</sub>Se<sub>5</sub>/ACGSe was above 57% in the wavelength range of 520–600 nm. The decrease below 540 nm is thought to be due to photo-absorption and recombination of photo-generated carriers in the CdS layer due to the low crystallinity,<sup>39,46</sup> which suggests the possibility of further improvement in this region of the spectrum by replacing CdS with a wider-band-gap material such as ZnS.<sup>44</sup> The IPCE for both Pt/CdS/CuGa<sub>3</sub>Se<sub>5</sub>/ACGSe and Pt/CdS/ACGSe converged to zero at *ca.* 760 nm, suggesting that the ACGSe layers act as photo-absorbers in both photocathodes. The photocurrent under the AM 1.5G spectrum estimated from the IPCE is consistent with the results of the *I*–*E* measurements (see Fig. S4 in ESI†).

To estimate the Faradaic efficiency of the Pt/CdS/CuGa<sub>3</sub>Se<sub>5</sub>/ACGSe photocathode for the generation of H<sub>2</sub> and O<sub>2</sub>, the gas products were analysed using micro-GC (see ESI†). Details of the measurement conditions are described in the ESI†. Fig. 3 shows the current–time curves at different potentials and the corresponding amounts of hydrogen and oxygen evolved on the specimen and Pt counter electrode. Two different applied potentials were used, namely 0 V<sub>RHE</sub> and 0.6 V<sub>RHE</sub>, and in both cases, stoichiometric hydrogen and oxygen evolution from water was confirmed, as shown in Fig. 3b and d. At 0.6 V<sub>RHE</sub>, a small decrease in the photocurrent was observed after 3 h (see Fig. 3c), likely due to the partial oxidation of CdS, because, at such a high potential, it may not be possible to maintain the entire surface of the CdS layers under reductive conditions.<sup>40</sup> The hydrogen and oxygen evolution at an applied potential of 0.6 V<sub>RHE</sub> was slightly lower than that estimated from the photocurrent. This might be due to degradation of the photocathode. The hydrogen evolution at 0.75 V<sub>RHE</sub> was further confirmed (see Fig. S5 in ESI†), which provides additional evidence for the contribution of the observed small photocurrent at a potential >0.6 V<sub>RHE</sub> to the hydrogen evolution reaction.

To assess the long-term stability of the prepared Pt/CdS/CuGa<sub>3</sub>Se<sub>5</sub>/ACGSe photocathode, the time course of the photocurrent was measured at 0 V<sub>RHE</sub> in a buffer solution under visible light irradiation, as shown in Fig. 4. After an induction period of a few days, the electrode showed a stable cathodic photocurrent for over 19 days without a detectable decrease. It should be noted that the observed fluctuations in the photocurrent during the measurements were due to the adsorption of bubbles of gas products on the photoelectrode and vigorous magnetic stirring.



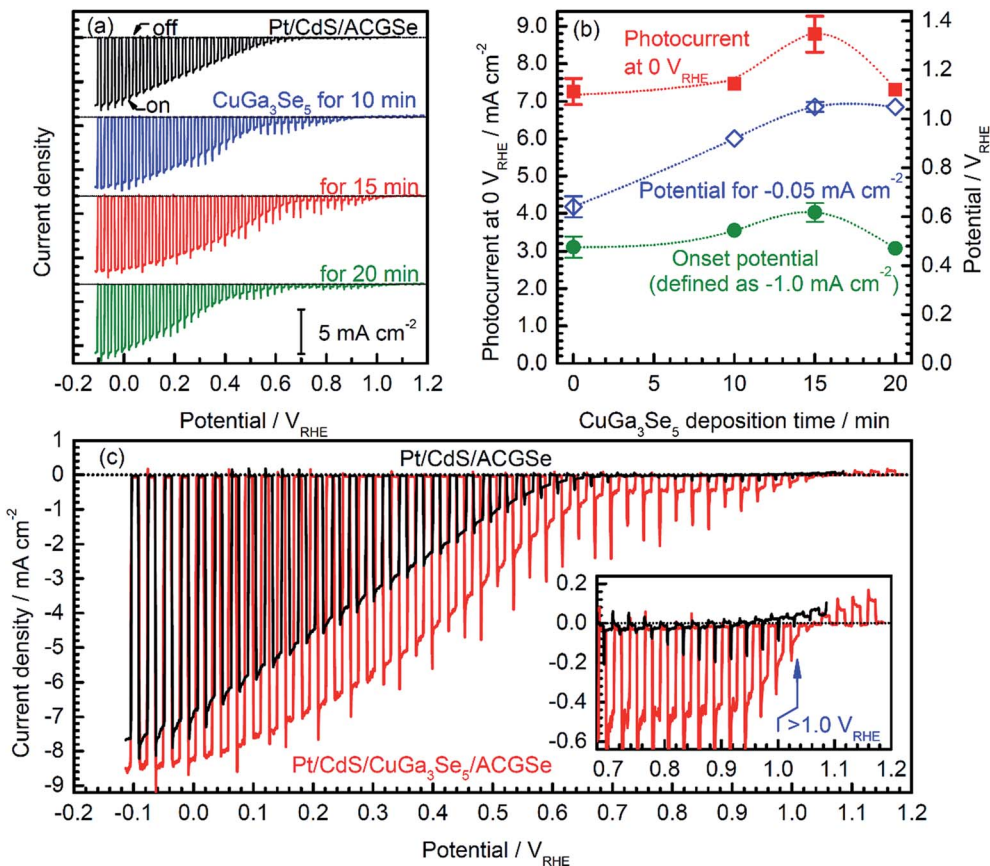


Fig. 1 Current–potential ( $I$ – $E$ ) curves for Pt/CdS/CuGa<sub>3</sub>Se<sub>5</sub>/ACGSe with various CuGa<sub>3</sub>Se<sub>5</sub> deposition times (a), plots of photocurrent density at 0 V<sub>RHE</sub> and onset potential against CuGa<sub>3</sub>Se<sub>5</sub> deposition time (b), and comparison of  $I$ – $E$  curves for Pt/CdS/ACGSe and Pt/CdS/CuGa<sub>3</sub>Se<sub>5</sub>/ACGSe with CuGa<sub>3</sub>Se<sub>5</sub> deposited for 15 min (c). A 0.1 M aqueous Na<sub>2</sub>HPO<sub>4</sub> solution (adjusted to pH 10 by addition of NaOH) was employed as the electrolyte. An applied potential was swept in the positive direction at 5 mV s<sup>-1</sup> under intermittent irradiation with simulated sunlight. Error bars show the standard deviation from the mean of the three samples.

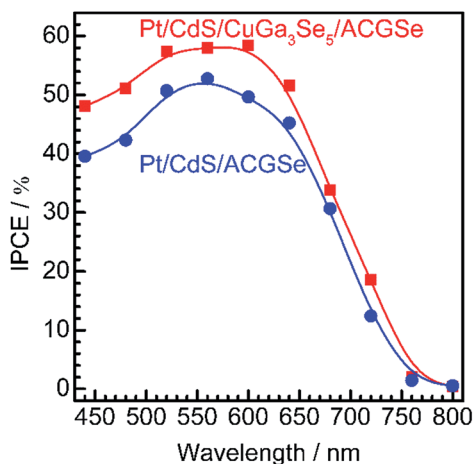


Fig. 2 Wavelength dependence of the IPCE spectra for Pt/CdS/CuGa<sub>3</sub>Se<sub>5</sub>/ACGSe with CuGa<sub>3</sub>Se<sub>5</sub> deposited for 15 min, and Pt/CdS/ACGSe measured at an applied potential of 0 V<sub>RHE</sub>. The IPCE was measured in 0.1 M Na<sub>2</sub>HPO<sub>4</sub> (adjusted to pH 10 by addition of NaOH) under monochromatic light from a 300 W Xe lamp equipped with band-pass filters and an optical fiber.

### Structural properties of the CuGa<sub>3</sub>Se<sub>5</sub>/ACGSe samples

To determine the structural properties of the electrodes, XRD, SEM, and TEM were conducted. XRD patterns for the CuGa<sub>3</sub>Se<sub>5</sub>/ACGSe with CuGa<sub>3</sub>Se<sub>5</sub> deposited on Mo/Ti/SLG for 15 min and a reference CuGa<sub>3</sub>Se<sub>5</sub> film deposited on Mo/Ti/SLG for 15 min are shown in Fig. 5. In addition to the markedly strong diffraction peaks associated with the Mo/Ti/SLG substrate, both samples showed a prominent peak at  $2\theta \approx 27$ – $28^\circ$ , assignable to the (112) diffraction from a chalcopyrite structure, suggesting that the preferred orientation was (112). The (112) diffraction peak for CuGa<sub>3</sub>Se<sub>5</sub>/ACGSe (Fig. 5b) exhibited a shoulder peak at *ca.*  $27.8^\circ$ , which corresponds to the (112) diffraction peak for CuGa<sub>3</sub>Se<sub>5</sub>.<sup>50,53,54</sup> This confirmed the presence of the CuGa<sub>3</sub>Se<sub>5</sub> layer. The differences in the diffraction angle and sharpness of the CuGa<sub>3</sub>Se<sub>5</sub> (112) peaks for CuGa<sub>3</sub>Se<sub>5</sub>/ACGSe and CuGa<sub>3</sub>Se<sub>5</sub> are due to intermixing at the CuGa<sub>3</sub>Se<sub>5</sub>/ACGSe interface and the different underlayers.

SEM images of the ACGSe and CuGa<sub>3</sub>Se<sub>5</sub>/ACGSe thin films are presented in Fig. 6. The ACGSe showed a rough surface consisting of large polygonal grains (see Fig. 6a), while CuGa<sub>3</sub>Se<sub>5</sub>/ACGSe showed a surface densely covered by flake-shaped grains (Fig. 6b), which is characteristic of CuGa<sub>3</sub>Se<sub>5</sub>.



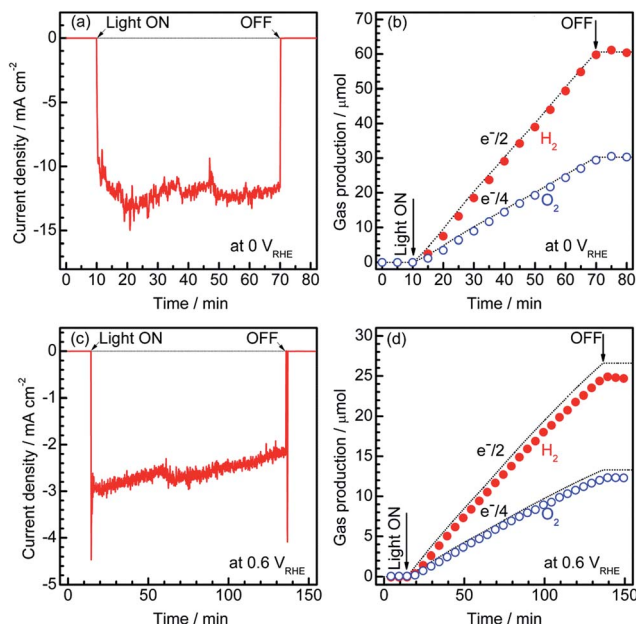


Fig. 3 Current–time curves for the Pt/CdS/CuGa<sub>3</sub>Se<sub>5</sub>/ACGSe electrode with CuGa<sub>3</sub>Se<sub>5</sub> deposited for 15 min at an applied potential of 0 V<sub>RHE</sub> (a) and 0.6 V<sub>RHE</sub> (c), and the corresponding amount of H<sub>2</sub> and O<sub>2</sub> that evolved during the measurements (b), (d). An airtight 3-electrode configuration was used, with a Pt wire and an Ag/AgCl electrode as the counter and reference electrodes, respectively. A 0.1 M Na<sub>2</sub>HPO<sub>4</sub> (adjusted to pH 10 by addition of NaOH) and a 150 W Xe lamp (420–800 nm) equipped with a cutoff filter (HOYA, L42) and a cold mirror (Optline, CM-1) were used as the electrolyte and light source, respectively. The dashed lines indicate the expected amounts of oxygen and hydrogen for a Faradaic efficiency of unity.



Fig. 4 Current–time curve for a Pt/CdS/CuGa<sub>3</sub>Se<sub>5</sub>/ACGSe electrode with CuGa<sub>3</sub>Se<sub>5</sub> deposited for 15 min at a potential of 0 V<sub>RHE</sub>. A buffer solution of 0.05 M Na<sub>2</sub>HPO<sub>4</sub> + 0.05 M NaH<sub>2</sub>PO<sub>4</sub> (adjusted to pH 7 by addition of NaOH) was used as the electrolyte. 420–800 nm light (100 W cm<sup>-2</sup>) from a Xe lamp equipped with a cutoff filter (HOYA, L42) and a cold mirror (Optline, CM-1) was employed as the light source.

(see Fig. S6 in ESI†).<sup>50,52</sup> This obvious difference in surface morphology implies that the CuGa<sub>3</sub>Se<sub>5</sub> layer fully covered the ACGSe underlayer. The cross-sectional SEM image of



Fig. 5 XRD patterns for CuGa<sub>3</sub>Se<sub>5</sub>/ACGSe with CuGa<sub>3</sub>Se<sub>5</sub> deposited for 15 min, and a reference CuGa<sub>3</sub>Se<sub>5</sub> film deposited on Mo/Ti/SLG for 15 min (a), and the corresponding (112) diffractions (b). The reference pattern for CGSe (PDF no. 31-456) is shown at the bottom for comparison.



Fig. 6 Top and cross-sectional SEM images of ACGSe (a) and (c), and CuGa<sub>3</sub>Se<sub>5</sub>/ACGSe with CuGa<sub>3</sub>Se<sub>5</sub> deposited for 15 min (b) and (d).

CuGa<sub>3</sub>Se<sub>5</sub>/ACGSe (Fig. 6d) clearly revealed the compact bilayer structure consisting of a CuGa<sub>3</sub>Se<sub>5</sub> overlayer and an ACGSe underlayer with columnar grains. The thickness of the CuGa<sub>3</sub>Se<sub>5</sub> layer was estimated from the SEM image to be about 100 nm, which is less than the thickness estimate of ca. 150 nm made on the basis of the deposition rate for the preparation conditions used. This discrepancy is indicative of interdiffusion between the CuGa<sub>3</sub>Se<sub>5</sub> and ACGSe layers, as revealed by the XRD results. It should be noted that the ACGSe layer in the ACGSe and CuGa<sub>3</sub>Se<sub>5</sub> samples was composed of large columnar grains, which is consistent with our previous report on ACGSe thin films.<sup>46</sup> It is well known that large columnar grains are desirable for efficient I-III-VI<sub>2</sub> thin-film solar cells.<sup>35–37</sup>





Fig. 7 Cross-sectional TEM images of CdS/CuGa<sub>3</sub>Se<sub>5</sub>/ACGSe sample with CuGa<sub>3</sub>Se<sub>5</sub> deposited for 15 min (a) and (b); EDX elemental maps for Cd (c), Ag (d), Cu (e), Ga (f), Se (g), Mo (h), Ti (i), Si (j); and line profiles for Cd, Cu and Ag across the CdS and CuGa<sub>3</sub>Se<sub>5</sub>/ACGSe interfaces (k). The red line in Fig. 4b indicates where the linear profile was measured. The sample was sliced using a Ga focused ion beam (FIB).

For the CdS-deposited CuGa<sub>3</sub>Se<sub>5</sub>/ACGSe sample, cross-sectional TEM and EDX mapping was conducted to characterize the interfacial structure. The cross-sectional TEM images (Fig. 7a and b) revealed a well-defined layered structure of CdS/CuGa<sub>3</sub>Se<sub>5</sub>/ACGSe/Mo/Ti/SLG, where Mo/Ti/SLG is the substrate. An EDX elemental map of Cd (Fig. 7c) clearly indicated that the CuGa<sub>3</sub>Se<sub>5</sub>/ACGSe surface was fully coated by a CdS layer with a thickness of *ca.* 80 nm. Fig. 7d–g show EDX elemental maps for Ag, Cu, Ga, and Se, and Fig. 7k shows line profiles for Cd, Cu, and Ag across the CdS and CuGa<sub>3</sub>Se<sub>5</sub>/ACGSe interfaces. From Fig. 7k, it can clearly be seen that Cd, Cu and Ag exhibited a concentration gradient, despite the pronounced Cd diffusion.<sup>55</sup> The concentration gradient for Cu corroborates the presence of a Cu-deficient ODC thin layer.

### Band alignments at solid–liquid interfaces

To elucidate the beneficial effects of the CuGa<sub>3</sub>Se<sub>5</sub> layer, the band alignment for the Pt/CdS/CuGa<sub>3</sub>Se<sub>5</sub>/ACGSe and Pt/CdS/ACGSe electrodes at solid–liquid interfaces were calculated numerically by solving the discretized Poisson's equation (see ESI†) as shown in Fig. 8.<sup>40</sup> For both samples, the width of the depletion layer formed at the solid–liquid interface under applied potentials of 0 V<sub>RHE</sub> and 0.6 V<sub>RHE</sub> was estimated to be 348 nm and 234 nm, respectively. Compared with the Pt/CdS/ACGSe electrode (Fig. 8b and d), the CuGa<sub>3</sub>Se<sub>5</sub>-modified sample had a more desirable stepped-down alignment of both the VBM and the conduction-band minimum (CBM) between the CdS and ACGSe layers, as shown in Fig. 8a and c, because the CuGa<sub>3</sub>Se<sub>5</sub> has a larger band gap and a deeper VBM potential than ACGSe (see Fig. S7–S9 in ESI†).

For the Pt/CdS/ACGSe electrode, photo-generated electron–hole pairs are created mainly within the depletion layer in the ACGSe, and then spatially separated by the built-in electric field, which can be described as band bending in a band diagram. The photo-generated electrons in the conduction band then have to pass through the defect-rich CdS/ACGSe interface, because of the



Fig. 8 Calculated band alignment near the solid–liquid interface for CdS/CuGa<sub>3</sub>Se<sub>5</sub>/ACGSe with CuGa<sub>3</sub>Se<sub>5</sub> deposited for 15 min, and Pt/CdS/ACGSe at an applied potential of 0 V<sub>RHE</sub> (a) and (b), and 0.6 V<sub>RHE</sub> (c) and (d). VBM, CBM and E<sub>F</sub> denote the valence-band maximum, conduction-band minimum, and Fermi energy, respectively.



large lattice mismatch and low crystallinity of CdS, in order to evolve hydrogen, while the photo-generated holes in the valence band move to the back contact layer (and finally to the counter electrode *via* the external circuit) for oxygen evolution. Considering this charge separation, it is possible that the CdS/ACGSe interface plays a key role in the recombination of photo-generated carriers.<sup>47,48</sup> One possible reason for the higher photocurrent and onset potential observed for Pt/CdS/CuGa<sub>3</sub>Se<sub>5</sub>/ACGSe than for Pt/CdS/ACGSe is a reduced amount of recombination at the interfaces. CuGa<sub>3</sub>Se<sub>5</sub> has almost the same crystal structure as ACGSe, except for the presence of ordered defect complexes and the absence of Ag (partially substituted for Cu in CuGaSe<sub>2</sub>) in the former. In addition, since the CuGa<sub>3</sub>Se<sub>5</sub> layer is deposited *in situ*, the quality of the CuGa<sub>3</sub>Se<sub>5</sub>/ACGSe interface is likely to be high. Since the CuGa<sub>3</sub>Se<sub>5</sub> interlayer has a deeper VBM potential than ACGSe, an energy barrier is formed that effectively prevents the diffusion of holes to the defective CdS/CuGa<sub>3</sub>Se<sub>5</sub> interface, thus suppressing carrier recombination. Note that the cathodic photocurrent at an applied potential of 0.6 V<sub>RHE</sub> is mainly due to photoexcited electrons generated in the CuGa<sub>3</sub>Se<sub>5</sub> layer, which is fully depleted and can absorb a portion of the incoming photons with an energy of >1.85 eV. Thus, the photo-excited carriers in the CuGa<sub>3</sub>Se<sub>5</sub> layers can directly contribute to the photocurrent in Pt/CdS/CuGa<sub>3</sub>Se<sub>5</sub>/ACGSe electrodes because of the presence of a strong built-in electric field and the step-like alignment of both the CBM and VBM.

## Conclusions

CuGa<sub>3</sub>Se<sub>5</sub>-modified ACGSe thin-film photocathodes modified with CdS and Pt were investigated for PEC hydrogen evolution from water under simulated sunlight irradiation. The photocurrent densities and onset potentials for Pt/CdS/CuGa<sub>3</sub>Se<sub>5</sub>/ACGSe photocathodes showed a strong dependence on the thickness of the CuGa<sub>3</sub>Se<sub>5</sub> layer. The Pt/CdS/CuGa<sub>3</sub>Se<sub>5</sub>/ACGSe photocathode with CuGa<sub>3</sub>Se<sub>5</sub> deposited for 15 min (*ca.* 100 nm) exhibited a cathodic photocurrent of 8.79 mA cm<sup>-2</sup> at 0 V<sub>RHE</sub>, an onset potential of 0.62 V<sub>RHE</sub> under simulated sunlight, and a HC-STH of 1.81% at 0.36 V<sub>RHE</sub>, which were higher than the values of 7.26 mA cm<sup>-2</sup>, 0.48 V<sub>RHE</sub>, and 1.02% for unmodified Pt/CdS/ACGSe. In addition, calculations showed that the inclusion of CuGa<sub>3</sub>Se<sub>5</sub> led to a more desirable band alignment near the solid-liquid interface because CuGa<sub>3</sub>Se<sub>5</sub> has a deeper VBM potential than ACGSe. A Pt/CdS/CuGa<sub>3</sub>Se<sub>5</sub>/ACGSe photocathode generated a stable photocurrent for *ca.* 20 days, producing stoichiometric hydrogen from water under visible light irradiation. These results demonstrate the feasibility of using CuGa<sub>3</sub>Se<sub>5</sub>-modified ACGSe electrodes decorated with CdS and Pt as photocathodes in dual-photoelectrode PEC cells for bias-free water splitting, though further improvements including realization of scalable and low cost electrodes by the fabrication methods like the simple particle transfer method are necessary.<sup>25,40</sup>

## Acknowledgements

This work was supported in part by a Grant-in-Aid for Specially Promoted Research (#23000009) of the Japan Society for the

Promotion of Science (JSPS). This work was also supported by the international exchange program of the A3 Foresight Program of the JSPS. A part of this work was conducted at the Research Hub for Advanced Nano Characterization, the University of Tokyo, under the support of the “Nanotechnology Platform” (project no. 12024046) by MEXT, Japan. L. Zhang acknowledges the China Scholarship Council (CSC) (no. 2011621015) for their scholarship support.

## Notes and references

- 1 N. Armaroli and V. Balzani, *Angew. Chem., Int. Ed.*, 2007, **46**, 52–66.
- 2 V. Balzani, A. Credi and M. Venturi, *ChemSusChem*, 2008, **1**, 26–58.
- 3 E. L. Wolf, *Nanophysics of Solar and Renewable Energy*, Wiley-VCH Verlag GmbH & Co. KGaA, 2012.
- 4 T. Hisatomi, J. Kubota and K. Domen, *Chem. Soc. Rev.*, 2014, DOI: 10.1039/c3cs60378d.
- 5 N. S. Lewis and D. G. Nocera, *Proc. Natl. Acad. Sci. U. S. A.*, 2006, **103**, 15729–15735.
- 6 R. M. Navarro, M. C. Alvarez-Galván, J. A. Villoria de la Mano, S. M. Al-Zahrani and J. L. G. Fierro, *Energy Environ. Sci.*, 2010, **3**, 1865–1882.
- 7 M. Grätzel, *Nature*, 2001, **414**, 338–344.
- 8 M. G. Walter, E. L. Warren, J. R. McKone, S. W. Boettcher, Q. Mi, E. A. Santori and N. S. Lewis, *Chem. Rev.*, 2010, **110**, 6446–6473.
- 9 Z. Li, W. Luo, M. Zhang, J. Feng and Z. Zou, *Energy Environ. Sci.*, 2013, **6**, 347–370.
- 10 M. S. Prévot and K. Sivula, *J. Phys. Chem. C*, 2013, **117**, 17879–17893.
- 11 B. A. Pinaud, J. D. Benck, L. C. Seitz, A. J. Forman, Z. Chen, T. G. Deutsch, B. D. James, K. N. Baum, G. N. Baum, S. Ardo, H. Wang, E. Miller and T. F. Jaramillo, *Energy Environ. Sci.*, 2013, **6**, 1983–2002.
- 12 S. Hu, C. Xiang, S. Haussener, A. D. Berger and N. S. Lewis, *Energy Environ. Sci.*, 2013, **6**, 2984–2993.
- 13 A. Fujishima and K. Honda, *Nature*, 1972, **238**, 37–38.
- 14 K. Sivula, R. Zboril, F. Le Formal, R. Robert, A. Weidenkaff, J. Tucek, J. Frydrych and M. Grätzel, *J. Am. Chem. Soc.*, 2010, **132**, 7436–7444.
- 15 K. Sivula, F. Le Formal and M. Grätzel, *ChemSusChem*, 2011, **4**, 432–449.
- 16 Q. Jia, K. Iwashina and A. Kudo, *Proc. Natl. Acad. Sci. U. S. A.*, 2012, **109**, 11564–11569.
- 17 E. A. Lladó, L. Chen, M. Hettick, N. Mashouf, Y. Lin, A. Javey and J. W. Ager, *Phys. Chem. Chem. Phys.*, 2014, **16**, 1651–1657.
- 18 E. L. Miller, B. Marsen, B. Cole and M. Lum, *Electrochem. Solid-State Lett.*, 2006, **9**, G248–G250.
- 19 S. J. Hong, H. Jun, P. H. Borse and J. S. Lee, *Int. J. Hydrogen Energy*, 2009, **34**, 3234–3242.
- 20 I. Thomann, B. A. Pinaud, Z. Chen, B. M. Clemens, T. F. Jaramillo and M. L. Brongersma, *Nano Lett.*, 2011, **11**, 3440–3446.
- 21 R. Abe, M. Higashi and K. Domen, *J. Am. Chem. Soc.*, 2010, **132**, 11828–11829.



- 22 Y. Li, L. Zhang, A. Torres-Pardo, J. M. González-Calbet, Y. Ma, P. Oleynikov, O. Terasaki, S. Asahina, M. Shima, D. Cha, L. Zhao, K. Takanebe, J. Kubota and K. Domen, *Nat. Commun.*, 2013, **4**, DOI: 10.1038/ncomms3566.
- 23 G. Liu, J. Shi, F. Zhang, Z. Chen, J. Han, C. Ding, S. Chen, Z. Wang, H. Han and C. Li, *Angew. Chem., Int. Ed.*, 2014, **53**, 7295–7299.
- 24 M. Higashi, K. Domen and R. Abe, *J. Am. Chem. Soc.*, 2013, **135**, 10238–10241.
- 25 T. Minegishi, N. Nishimura, J. Kubota and K. Domen, *Chem. Sci.*, 2013, **4**, 1120–1124.
- 26 M. J. Kenney, M. Gong, Y. Li, J. Z. Wu, J. Feng, M. Lanza and H. Dai, *Science*, 2013, **342**, 836–840.
- 27 Y. W. Chen, J. D. Prange, S. Dühnen, Y. Park, M. Gunji, C. E. D. Chidsey and P. C. McIntyre, *Nat. Mater.*, 2011, **10**, 539–544.
- 28 M. H. Lee, K. Takei, J. Zhang, R. Kapadia, M. Zheng, Y.-Z. Chen, J. Nah, T. S. Matthews, Y.-L. Chueh, J. W. Ager and A. Javey, *Angew. Chem., Int. Ed.*, 2012, **51**, 10760–10764.
- 29 H. Wang, T. Deutsch and J. A. Turner, *J. Electrochem. Soc.*, 2008, **155**, F91–F96.
- 30 A. Paracchino, V. Laporte, K. Sivula, M. Grätzel and E. Thimsen, *Nat. Mater.*, 2011, **10**, 456–461.
- 31 A. Paracchino, N. Mathews, T. Hisatomi, M. Stefiak, S. D. Tilley and M. Grätzel, *Energy Environ. Sci.*, 2012, **5**, 8673–8681.
- 32 B. Seger, T. Pedersen, A. B. Laursen, P. C. K. Vesborg, O. Hansen and I. Chorkendorff, *J. Am. Chem. Soc.*, 2013, **135**, 1057–1064.
- 33 Q. Ding, F. Meng, C. R. English, M. C.-Acevedo, M. J. Shearer, D. Liang, A. S. Daniel, R. J. Hamers and S. Jin, *J. Am. Chem. Soc.*, 2014, **136**, 8504–8507.
- 34 M. Bär, W. Bohne, J. Röhrich, E. Strub, S. Lindner, M. C. Lux-Steiner, Ch.-H. Fischer, T. P. Niesen and F. Karg, *J. Appl. Phys.*, 2004, **96**, 3857–3860.
- 35 P. Jackson, D. Hariskos, E. Lotter, S. Paetel, R. Wuerz, R. Menner, W. Wischmann and M. Powalla, *Prog. Photovoltaics*, 2011, **19**, 894–897.
- 36 I. Repins, M. A. Contreras, B. Egaas, C. DeHart, J. Scharf, C. L. Perkins, B. To and R. Noufi, *Prog. Photovolt.: Res. Appl.*, 2008, **16**, 235–239.
- 37 S. Niki, M. Contreras, I. Repins, M. Powalla, K. Kushiya, S. Ishizuka and K. Matsubara, *Prog. Photovoltaics*, 2010, **18**, 453–466.
- 38 B. Marsen, B. Cole and E. L. Miller, *Sol. Energy Mater. Sol. Cells*, 2008, **92**, 1054–1058.
- 39 M. Moriya, T. Minegishi, H. Kumagai, M. Katayama, J. Kubota and K. Domen, *J. Am. Chem. Soc.*, 2013, **135**, 3733–3735.
- 40 H. Kumagai, T. Minegishi, Y. Moriya, J. Kubota and K. Domen, *J. Phys. Chem. C*, 2014, **118**, 16386–16392.
- 41 <http://rredc.nrel.gov/solar/spectra/am1.5/ASTMG173/ASTMG173.html>.
- 42 D. Yokoyama, T. Minegishi, K. Maeda, M. Katayama, J. Kubota, A. Yamada, M. Konarai and K. Domen, *Electrochem. Commun.*, 2010, **12**, 851–853.
- 43 D. Yokoyama, T. Minegishi, K. Jimbo, T. Hisatomi, G. Ma, M. Katayama, J. Kubota, H. Katagiri and K. Domen, *Appl. Phys. Express*, 2010, **3**, 101202.
- 44 S. Ikeda, T. Nakamura, S. M. Lee, T. Yagi, T. Harada, T. Minegishi and M. Matsumura, *ChemSusChem*, 2011, **4**, 262–268.
- 45 S. Ikeda, M. Nonogaki, W. Septina, G. Gunawan, T. Harada and M. Matsumura, *Catal. Sci. Technol.*, 2013, **3**, 1849–1854.
- 46 L. Zhang, T. Minegishi, J. Kubota and K. Domen, *Phys. Chem. Chem. Phys.*, 2014, **16**, 6167–6174.
- 47 V. Nadenau, U. Rau, A. Jasenek and H. W. Schock, *J. Appl. Phys.*, 2000, **87**, 584–593.
- 48 M. Saad and A. Kassis, *Sol. Energy Mater. Sol. Cells*, 2011, **95**, 1927–1931.
- 49 M. Rusu, S. Wiesner, R. Würz, S. Lehmann, S. Doka-Yamigno, A. Meeder, D. F. Marrón, M. Bär, V. Koteski, H. E. Mahnke, E. Arushanov, J. Beckmann, K. Höhn, W. Fritsch, W. Bohne, P. Schubert-Bischoff, M. Heuken, A. Jäger-Waldau, A. Rumberg and T. Schedel-Niedrig, *Sol. Energy Mater. Sol. Cells*, 2011, **95**, 1555–1580.
- 50 J. Kim, T. Minegishi, J. Kubota and K. Domen, *Jpn. J. Appl. Phys.*, 2012, **51**, 15802.
- 51 C. Rincón, S. M. Wasim, G. Marín, E. Hernández, G. S. Perez and J. Galibert, *J. Appl. Phys.*, 2000, **87**, 2293–2296.
- 52 J. Kim, T. Minegishi, J. Kubota and K. Domen, *Energy Environ. Sci.*, 2012, **5**, 6368–6374.
- 53 S. Lehmann, M. Bär, D. F. Marrón, P. Pistor, S. Wiesner, M. Rusu, I. Kötschau, I. Lauermann, A. Grimm, S. Sokoll, Ch.-H. Fischer, T. Schedel-Niedrig, M. C. Lux-Steiner and C. Jung, *Thin Solid Films*, 2006, **511–512**, 623–627.
- 54 R. Caballero, C. A. Kaufmann, V. Efimova, T. Rissom, V. Hoffmann and H. W. Schock, *Prog. Photovoltaics*, 2013, **21**, 30–46.
- 55 M. Rusu, M. Bär, S. Lehmann, S. Sadewasser, L. Weinhardt, C. A. Kaufmann, E. Strub, J. Röhrich, W. Bohne, I. Lauermann, Ch. Jung, C. Heske and M. Ch. Lux-Steiner, *Appl. Phys. Lett.*, 2009, **95**, 173502.

